1	Performance Modeling of a Diode-Laser-Based
2	Direct Detection Doppler Lidar for Vertical Wind Profiling
3	
4	Kevin S. Repasky, ^a Owen Cruikshank, ^a and Luke Colberg ^a
5	^a Department of Electrical and Computer Engineering, Montana State University, Bozeman, Montana
6	
7	Corresponding author: Kevin S. Repasky, repasky@montana.edu

8 ABSTRACT

Micropulse differential absorption lidar (MPD) for water vapor, temperature, and aerosol profiling have been developed, demonstrated, and are addressing the needs of the atmospheric science community for low-cost ground-based networkable instruments capable of long-term monitoring of the lower troposphere. The MPD instruments use a diode-laser-based (DLB) architecture that can easily be adapted for a wide range of applications. In this study, a DLB direct detection Doppler lidar based on the current MPD architecture is modeled to better understand the efficacy of the instrument for vertical wind velocity measurements with the long-term goal of incorporating these measurements into the current network of MPD instruments. The direct detection Doppler lidar is based on a double-edge receiver that utilizes two Fabry-Perot interferometers and a vertical velocity retrieval that requires the ancillary measurement of the backscatter ratio, which is the ratio of the total backscatter coefficient to the molecular backscatter coefficient. The modeling in this paper accounts for the major sources of error. It indicates that the vertical velocity can be retrieved with an error of less than 0.56 m s⁻¹ below 4 km with a 150-m range resolution and an averaging time of five minutes.

SIGNIFICANCE STATEMENT

Monitoring the temperature, relative humidity, and winds in the lower atmosphere is important for improving weather forecasting, particularly for severe weather such as thunderstorms. Cost-effective MicroPulse DIAL (MPD) instrumentation for continuous temperature and humidity monitoring has been developed and demonstrated, and its effects on weather forecasting are currently being evaluated. The modeling study described in this paper studies the feasibility of using a similar cost-effective MPD instrument architecture for monitoring vertical wind velocity in the lower atmosphere. Modeling indicates that wind velocities can be measured with less than 0.56 m s⁻¹ accuracy and demonstrates the feasibility of adding vertical wind velocity measurements to the MPD instruments.

1. Introduction

Winds play an essential role in many atmospheric phenomena such as convection, turbulence, and instability. They also influence the coupling of the lower atmosphere and the underlying surface through momentum, energy, and the mixing and transport of trace gas constituents and aerosols (Wallace and Hobbs 2006). The ability to measure atmospheric

winds is important for understanding the state of the atmosphere and can lead to an improved understanding of atmospheric dynamics and climate processes. Furthermore, the ability to measure and assimilate winds using a ground-based network of instruments can improve the predictive capabilities of numerical weather forecasting (Zhao et al. 2006).

Lidar has been demonstrated as a means of monitoring atmospheric winds (Weitkamp 2006; Reitebuch 2012). These lidar instruments depend on the Doppler effect that shifts the spectra of the backscattered light with a spectral shift proportional to the radial (line of sight) wind velocity. The ability to measure the Doppler shift associated with the scattered light is typically achieved using one of two methods referred to as the coherent (heterodyne) and direct detection (incoherent) techniques (Weitkamp 2006; Reitebuch 2012). Both the coherent and direct detection Doppler lidar techniques have advantages and disadvantages that must be addressed while implementing these techniques.

The coherent Doppler lidar technique measures the Doppler shift by mixing the backscatter signal with a reference signal to create a beat signal. The beat signal is then used to infer the Doppler shift, which is related to the radial velocity. Early coherent Doppler lidar instruments operated at a 10-µm wavelength (Post et al. 1982; Bilbro et al. 1986), with more recent coherent Doppler lidar instruments operating at shorter wavelengths (Post et al. 1982; Bilbro et al. 1986; Grund et al. 2001; Schroeder et al. 2020; Koch et al. 2007; Emmitt et al. 2005; Kavaya et al. 2014; Abdelazim et al. 2015; Schwiesow and Spowart 1996; Rodrigo and Pederson 2012). Coherent Doppler lidar have good spatial and temporal resolution and can retrieve the radial velocity with high precision. Laser transmitters for coherent Doppler lidar instruments such as the Doppler Aerosol WiNd (DAWN) lidar (Kavaya et al. 2014) and the German Aerospace Center [Deutsches Zentrum für Luft- und Raumfahrt (DLR)] coherent Doppler wind lidar (Witschas et al. 2017) typically use custom solid-state lasers operating near 2 µm for eye-safe operations. Coherent Doppler lidar instruments can provide wind velocity measurements in both aerosol-rich regions (Turk et al. 2020) and regions where molecular scattering dominates (Witschas et al. 2017; Bedka et al. 2021).

The direct detection Doppler lidar technique utilizes a frequency discriminating component in the optical receiver such as a Fabry Perot (McKay 1998) or Mach-Zehnder (Bruneau 2001) interferometer to ascertain the Doppler shift. The direct detection Doppler lidar can retrieve the vertical wind velocity in regions with and without aerosol loading. However, care must be taken to account for the linewidth of the backscattered light resulting

- from heavier aerosols and lighter atmospheric molecules, the latter of which will broaden the
- backscatter signal. Furthermore, direct detection lidar requires a stable laser transmitter and a
- stable frequency discriminator in the optical receiver to retrieve the wind velocity accurately
- via the Doppler shift. Several ground-based, aircraft-based, and, most recently, satellite-based
- direct detection Doppler wind lidar instruments are in operation (Tucker et al. 2018; Gentry
- et al. 2011; Reitebuch et al. 2009; Paffrath et al. 2009; Straume et al. 2020; Kanitz et al.
- 77 2020; Reitebuch et al. 2020; Irgang et al. 2020; Gentry and Chen 2003; Gentry and Chen
- 78 2002; Werner et al. 2001; Xia et al. 2007; Shen et al. 2008).
- 79 Commercial Doppler wind lidar instruments are available (Ando et al. 2008; Dai et al.
- 80 2020). These instruments have proven valuable for the wind energy community (Cheng et al.
- 81 2017; Kosovic et al. 2020; Al-Yahyai et al. 2010). Furthermore, they have been used in
- several atmospheric science campaigns (Schween et al. 2014; Banakh and Smalikho 2016;
- 83 Bell et al. 2020). These instruments operate with a wavelength near 1.5 μm and can provide
- 3D wind fields using a scanning technique. However, the range of these instruments is
- 85 typically limited to regions of high aerosol loading. Because these instruments rely on aerosol
- scattering, they have difficulty retrieving winds above the capping inversion and may be
- unable to address issues like the transport of aerosols and pollutants into the free troposphere.
- Researchers at Montana State University (MSU) and the National Center for Atmospheric
- 89 Research (NCAR) are developing diode-laser-based (DLB) remote sensing instruments for
- 90 thermodynamic and aerosol profiling in the lower troposphere. Currently, a network of five
- 91 micropulse differential absorption lidar (MPD) instruments for monitoring atmospheric water
- 92 vapor is operational (Spuler et al. 2015; Spuler et al. 2021). Three DLB high spectral
- 93 resolution lidar (HSRL) are also operational (Hayman and Spuler 2017), and two MPD
- 94 instruments for temperature profiling are under development (Bunn et al. 2018; Repasky et
- al., 2019; Stillwell et al., 2020). The DLB MPD and HSRL instruments have demonstrated
- long-term autonomous operation, are cost-effective, and can be used as a ground-based
- 97 network of thermodynamic profiling lidar. Such a network could address the needs of the
- 98 weather forecasting and climate science communities expressed in National Research Council
- 99 reports (2009; 2010), a National Academies of Sciences, Engineering, and Medicine report
- 100 (2018), and discussed in the literature (Bell et al. 2020; Wulfmeyer et al. 2015).
- The DLB architecture of the current MPD and HSRL instruments provides flexibility
- which allows easy adaptability for various lidar applications. In this paper, a DLB direct

detection Doppler wind lidar for vertical wind profiling based on a double-edge technique and an ancillary HSRL measurement of the backscatter ratio, the ratio of the total backscatter to the molecular backscatter, is modeled. The ancillary measurement of the backscatter ratio allows the spectral distribution of the backscatter signal to be used in the vertical velocity retrieval. The effects of major sources of error on the retrieved vertical velocity are estimated to address if a DLB direct detection Doppler wind lidar can add a capability to the thermodynamic profiling network being developed. These sources of error include Poisson noise associated with the photon counting used in the DLB instrument, the laser frequency stability, the etalon stability, the uncertainty in the ancillary backscatter ratio measurement, and the uncertainty in the atmospheric parameters assumed in the HSRL retrieval.

The proposed direct detection Doppler wind lidar modeled in this paper has the potential to add vertical wind velocity measurements to the current MPD instruments. Vertical winds range between 0.1 m s⁻¹ and 1 m s⁻¹ for fair weather conditions and up to 5 m s⁻¹ in complex terrain where orographic lifting is significant. Vertical wind measurements combined with the existing capability of the MPD instruments to measure humidity, temperature, and boundary layer structure using aerosol profiling, address the needs of the scientific community. Current research with numerical weather forecasting models uses continuous humidity profiles provided by the network of MPD instruments to improve mesoscale weather predictions for events such as thunderstorms and precipitation patterns. Providing continuous vertical wind profiles to the numerical weather forecasting models has the potential to improve the accuracy of these models further.

This paper is organized as follows. The theory for the vertical velocity retrieval that incorporates the backscatter lineshape is presented in section 2. The proposed instrument is discussed in section 3. The performance modeling is presented in section 4. In section 5, uncertainty in the retrieved vertical velocity is discussed. Finally, some brief concluding remarks are presented in section 6.

2. Theory

The goal of the DLB Doppler wind lidar is to determine the frequency shift of the backscattered light resulting from the Doppler effect, Δf . The frequency shift can then be related to the radial velocity, v_r , using $v_r = \lambda_0 \Delta f/2$ with λ_0 representing the wavelength of the lidar laser transmitter.

The return signal, $N_x(r, f)$, can be calculated as a function of range, r, and frequency, f, using the lidar equation from Kovalev and Eichinger (2004).

$$N_{x}(r,f) = N_{0} \frac{c\tau}{2} \frac{A_{0}}{r^{2}} \beta(r,f) T_{atm}^{2}(r) O(r) \varepsilon_{x} T_{e,x}(f)$$

$$\tag{1}$$

- The term N_0 is the number of photons per pulse leaving the laser transmitter, c is the speed of
- light, τ is the pulse duration, A_0 is the telescope area, $\beta(r, f)$ is the total backscatter, $T_{atm}(r)$
- is the atmospheric transmission, O(r) is the overlap function, ε_x is the receiver efficiency,
- 140 $T_{e,x}(f)$ is the etalon transmission. The variable x can take on values of a and b depending on
- which of the two receiver channels is being modeled.
- The total backscatter can be written as

$$\beta(r,f) = \beta_a(r)\delta(f_0 + \Delta f - f) + \beta_m(r)g(r,f_0 + \Delta f,f)$$
 (2)

- where $\beta_a(r)$ is the aerosol backscatter, $\beta_m(r)$ is the molecular backscatter, f_0 is the laser
- transmitter operating frequency, Δf is the Doppler induced shift, $\delta(f_0 + \Delta f f)$ is a delta
- 146 function that sets the frequency of the aerosol backscatter signal to $f = f_0 + \Delta f$, and
- 147 $g(r, f_0 + \Delta f, f)$ is the Doppler-broadened lineshape centered at $f_0 + \Delta f$. The assumption
- was made that the outgoing laser transmitter pulse and the aerosol backscatter signal can be
- treated as a delta function with the frequency $f = f_0 + \Delta f$. The Doppler-broadened lineshape
- is normalized so that $\int g(r, f_0 + \Delta f, f) df = 1$.
- The backscatter ratio, B(r), is defined as

$$B(r) = \frac{\beta_a(r) + \beta_m(r)}{\beta_m(r)} \tag{3}$$

- and can be measured using the HSRL technique (Shipley et al. 1983; Hair et al. 2008;
- 154 Esselborn et al. 2008; Hayman and Spuler 2017). The return signal as a function of range and
- 155 frequency can be written using the molecular backscatter and the backscatter ratio

156
$$N_{x}(r,f) = F(r)\varepsilon_{x}[(B(r)-1)\delta(f_{0} + \Delta f - f) + g(r,f_{0} + \Delta f,f)]T_{e,x}(f)$$
 (4)

157 where

158
$$F(r) = N_0 \frac{c\tau}{2} \frac{A_0}{r^2} \beta_m(r) T_{atm}^2(r) O(r).$$
 (5)

The total return signal, $N_x(r)$, as a function of range is found by integrating over frequency.

160
$$N_{x}(r) = F(r)\varepsilon_{x}[(B(r) - 1)T_{e,x}(f = f_{0} + \Delta f) + \int g(r, f_{0} + \Delta f, f)T_{e,x}(f)df]$$
 (6)

The double-edge direct detection Doppler wind lidar utilizes the etalons in the receiver channels *a* and *b* with their center frequencies offset to measure the Doppler shift. A differential measurement is then completed based on the return signals in channels *a* and *b* so that the Doppler direct detection signal is

165
$$M(r) = \frac{N_a(r) - N_b(r)}{N_a(r) + N_b(r)}$$
 (7)

which can be written

$$M(r) = \frac{(B(r)-1)(\varepsilon_a T_{e,a}(f=f_0+\Delta f)-\varepsilon_b T_{e,b}(f=f_0+\Delta f))+\int g(r,f_0+\Delta f,f)(\varepsilon_a T_{e,a}(f)-\varepsilon_b T_{e,b}(f))df}{(B(r)-1)(\varepsilon_a T_{e,a}(f=f_0+\Delta f)+\varepsilon_b T_{e,b}(f=f_0+\Delta f))+\int g(r,f_0+\Delta f,f)(\varepsilon_a T_{e,a}(f)+\varepsilon_b T_{e,b}(f))df}$$
(8)

The Doppler frequency shift is determined as follows. For a given backscatter ratio, B(r), (8) can be used to calculate the expected direct detection signal as a function of frequency shift, Δf . The retrieved Doppler frequency shift is the frequency shift that minimizes the difference between the measured direct detection signal based on the measured return signal from channels a and b used in (7) and the calculated direct detection signal from (8).

The atmospheric model used for the following numerical calculations consists of a temperature profile, $T(r) = T_s + \gamma r$, with a surface temperature of $T_s = 300 \, K$ and a lapse rate of $\gamma = -6.5 \, K \, km^{-1}$. The pressure as a function of range, P(r), is found using the relationship $P(r) = P_s[T_s/T(r)]^{-5.2199}$ where a surface pressure of $P_s = 1 \, atm$ was used (Kovalev and Eichinger 2004). The molecular backscatter was calculated using the model presented in Kovalev and Eichinger (2004), and the Doppler-broadened lineshape, D(r, f), is calculated using

180
$$D(r,f) = \sqrt{\frac{mc^2}{8\pi kT(r)f_0^2}} exp\left(-\frac{mc^2}{8kT(r)f_0^2}(f - f_0)^2\right)$$
 (10)

where m is the mass of an average air molecule and k is the Boltzmann constant (Shipley et al. 1983). Finally, the backscatter ratio, B(r), used for modeling is shown in Fig. 1. The planetary boundary layer height is located at a range of 1.5 km, and the maximum value of the backscatter ratio is 2.05. This backscatter ratio is typical of the backscatter ratio observed at MSU using an MPD instrument operating at 770 nm (Stillwell et al. 2020). The typical planetary boundary layer height observed at MSU ranges between 0.5 and 3 km and the backscatter ratio within the boundary layer ranges from 1.5 to 2.5, with higher values resulting from forest fire smoke in the late summer (Colberg et al. 2022).

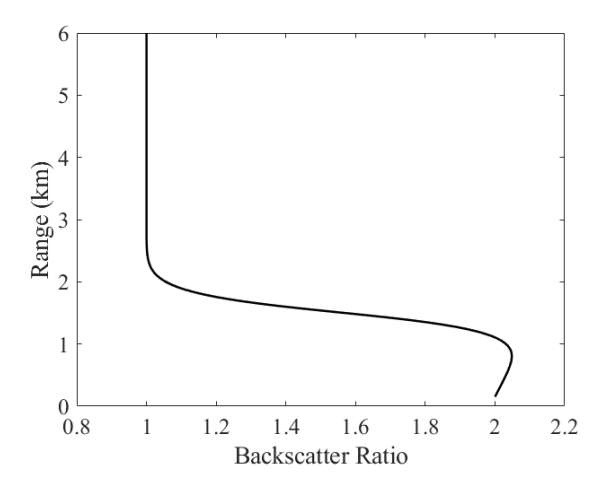


Fig. 1. The backscatter ratio used in the numerical modeling of the DLB direct detection Doppler wind lidar. This modeled backscatter ratio is based on backscatter ratio measurements made at 770 nm using an MPD instrument that has provided data over the past year.

3. Proposed instrument

The DLB MPD architecture has led to the successful development of several DIAL and HSRL instruments (Nehrir et al. 2009; Nehrir et al. 2011; Nehrir et al. 2012; Spuler et al. 2015; Hayman and Spuler 2017; Repasky et al. 2019; Stillwell et al. 2020; Spuler et al. 2021). This architecture uses continuous wave (cw) tunable diode lasers, amplifiers that are commercially available in the near-infrared spectral region (700 - 1000 nm), and siliconbased single-photon-counting modules (SPCMs) with high quantum efficiencies, large dynamic ranges, and low dark count rates. The DLB architecture provides flexibility that allows easy adaptability for direct detection Doppler wind lidar measurements.

A schematic of the proposed instrument is shown in Fig. 2. A fiber-coupled distributed Bragg reflector (DBR) laser operating at 780 nm is used as a seed laser for the Doppler wind measurements (green box and dot-dot-dashed line). The output is split using a fiber tap, with 10% of the light sent to a second fiber tap. The second tap splits the light equally, with one output directed to a wavemeter for coarse wavelength locking and the second output directed to a rubidium (RB) absorption cell for fine wavelength locking. This locking scheme is discussed further in section 5e. The remaining 90% of the light from the first fiber tap directs the light to a polarization controller, an optical isolator, and a half-wave plate. The optical isolator prevents optical feedback from affecting the DBR laser, while the polarization controller and half-wave plate ensure the appropriate polarization is achieved for injection seeding the tapered semiconductor optical amplifier (TSOA). The TSOA is driven with a

pulsed current controller and generates the pulse train. The output from the TSOA is collimated and incident on a dichroic beam combiner (BC).

A second fiber-coupled DBR laser operating at 770 nm (red box with dotted red line) is used for the HSRL measurement. The output is split using a fiber tap, with 10% of the output directed to a wavemeter for wavelength locking. The remaining 90% of the light is directed to a polarization controller, an isolator, and a half-wave plate and is coupled into a TSOA. The pulse current driver is used to create a pulse train. The output from the TSOA is collimated and directed to the BC.

The 770-nm and 780-nm beams are combined using a dichroic beam combiner. The combined beam passes through a matched axicon pair, creating a collimated annular beam. This beam passes through a borehole in an elliptic transmit/receive (T/R) mirror. A lens is used to couple the annular beam to the inner half of the 40-cm diameter F/3 telescope. The telescope has a 10 cm diameter secondary mirror. The outgoing beam has an annular shape with a 10 cm inner diameter and 20 cm outer diameter. The light scattered in the atmosphere is collected by the outer half of the telescope (between a 20 cm diameter and 40 cm diameter) is reflected by the T/R mirror, and coupled into a multimode optical fiber with a core diameter of 105 µm. The output from the multimode optical fiber is collimated, and the combined beam is then incident on a dichroic beam splitter (BS) that separates the 770-nm and 780-nm signals.

The backscatter signal at 780 nm passes through the BS and is incident on two narrowband filters with a passband of 0.75 nm. After the narrowband filters, the beam is incident on a 50/50 beam splitting cube (BSC) with half of the light directed to etalon a and half of the light directed to etalon b. After each etalon, the light is coupled into multimode optical fibers that deliver the light to SPCMs consisting of avalanche photodiodes (APDs) operating in Geiger mode and the electronic circuitry. This receiver path is used for the direct detection Doppler wind velocity measurements.

The 770-nm light reflected from the BS passes through two narrowband optical filters with a 0.75-nm bandpass and an etalon used to suppress background light. The light is then incident on a BSC with the light passing through the BSC coupled into a multimode optical fiber and monitored using an SPCM. The light reflected by the BSC is incident on a potassium (K) absorption cell used as a filter to block the aerosol backscatter signal while allowing some of the Doppler-broadened molecular backscatter signal to pass. This light is

then coupled into a multimode optical fiber and monitored using an SPCM. The HSRL measurement is made using this 770-nm channel. This design is similar to an operational MPD instrument used for measuring water vapor, temperature, and quantitative aerosol backscatter simultaneously (Repasky et al. 2019; Stillwell et al. 2020). The performance parameters for the proposed Doppler wind lidar channel (the 780-nm channel) are provided in Table 1. They are based on current MPD instruments and are used to model the proposed instrument performance. The receiver efficiency includes the fiber coupling, the detector quantum efficiency, and the optical transmission of all components in the receiver channel at 780 nm except for the BSC and is based on experience with current MPD instruments.

The background counts, N_b , from solar radiation can be estimated as (Spuler et al. 2015)

$$N_b = S_b \Omega_t \Delta f A_r \eta_r \eta_d \frac{\lambda}{hc}$$
 (11)

where S_b is the sky radiance, Ω_t is the receiver field of view, Δf is the effective filter bandwidth, η_r is the receiver optical efficiency, η_d is the detector quantum efficiency, λ is the laser wavelength, and h is Planck's constant. For a daytime sky radiance of $S_b = 1.15 \times 10^{-3} \ W \ cm^{-2} \ \mu m^{-1} \ Sr^{-1}$ and the instrument parameters presented in Table 1, the background count rate is 91 kHz. The count rate resulting from the solar background is well within the linear operating regime of the SPCM, which typically occurs below 1 MHz. The background count rate can be accounted for using a background subtraction algorithm in the retrieval program.

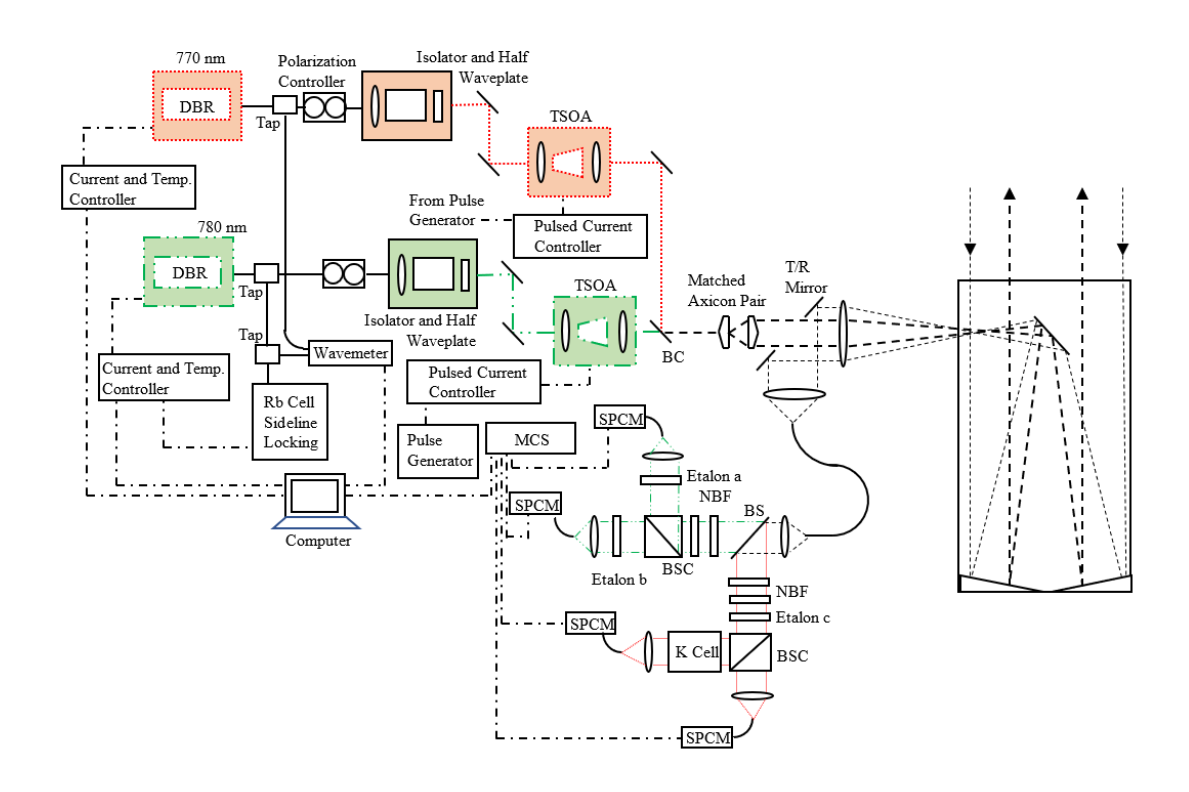


Fig. 2. Schematic of the proposed DLB direct detection Doppler wind lidar instrument. Dashed lines indicate optical paths, solid lines indicate fiber optical cables, and dot-dashed lines represent electrical cables. The green boxes and lines corresponds to the 780 nm wavelength while the orange boxes and lines correspond to the 770 nm wavelength.

Transmitter	Specification	Narrowband Filters	
Wavelength	780 nm	Interference Filter	750 pm
		Bandwidth	_
Linewidth	< 1 MHz	Effective Filter bandwidth	40 pm
Pulse Energy	5 μJ	Receiver	Specification
Pulse Duration	1 μs	Outer (inner) diameter	40.6 cm (20.3 cm)
Pulse Repetition Rate	10 kHz	Area	970 cm^2
Spectral Purity	> 99.5%	Field of View	115 µrad
Laser Divergence	60 μrad	Receiver Efficiency	10%
Etalons		Unambiguous Range	15 km
Free Spectral Range	100 pm	Detectors	SPCM
Finesse	20	Quantum Efficiency	50 %
Beam Divergence at	1.3 mrad	Dark Count Rate	200 counts s ⁻¹
Etalon			
		Dead Time	50 ns

Table 1. Instrument parameters used for modeling.

Several options exist for determining the spectral shift of the scattered light based on a frequency discriminator. For the design discussed above, a beam splitter directs the 780-nm light in the receiver to two separate etalons with an offset in their resonant frequencies. The advantage of this method is the commercial availability of fused silica solid etalons that use a

substrate with dielectric coatings to form the interferometer. The proposed interferometers are similar to those currently used in the MPDs for water vapor and temperature profiling. These etalons are tuned and stabilized using commercially available temperature controls and have been successfully deployed over long timeframes (months to a year) at unattended field deployments. However, the use of the etalons as the frequency discriminator has the disadvantage of the signal at each detector being reduced by 50% because of the 50/50 beam splitter, which lowers the signal-to-noise performance. A second option for the frequency discriminator is using a technique similar to that used in the Airborne Demonstrator for Direct-Detection Doppler wind lidar (ALADIN) (Reitebuch et al. 2009). Using a series of polarizers and waveplates, light rejected from the first interferometer is sent into the second interferometer allowing the maximum signal to be incident on each of the two interferometers. This optical setup is more efficient than the proposed optical discriminator that uses a 50/50 beamsplitter and two etalons. However, because of the design of the offset and bandpass of the two etalons in the proposed design, there is overlap in the transmission spectra of the two etalons making the implementation of an optical system similar to ALADIN difficult to implement.

4. Performance modeling

The DLB direct detection wind lidar for measuring winds in the lower troposphere needs to be able to measure winds within the aerosol-dense planetary boundary layer as well as above the capping inversion, where scattering results predominately from atmospheric molecules. A plot of transmission as a function of frequency for the two etalons is shown in Fig. 3 as the solid and dotted black lines. The frequency offset of the etalons is defined as the absolute value of the frequency difference, $f_c - f_0$, where f_c is the center frequency associated with the etalon transmission peak. The molecular backscatter for a Doppler-broadened lineshape for a 300-K temperature is shown as the red dot-dashed line. The red dotted vertical line indicates the laser lineshape, which has the same lineshape as the aerosol backscatter. From Fig. 3, the design tradeoffs for the etalon bandwidth and frequency offset can be seen. The smaller the bandpass of the etalons, the larger the change in the signal, M(r), will be for a given Doppler frequency shift. However, as the bandpass of the etalons decreases, the return signal in each channel will also decrease. These smaller signals result in lower signal-to-noise ratios (SNRs) due to the Poisson noise associated with photon counting and larger uncertainty in the retrieved vertical velocity. The frequency offset is also an important factor

in determining the performance of the DLB Doppler wind lidar. If the offset is too large, the return signals will operate in the wings of the etalon transmission, resulting in both a low signal and a small change in the signal, M(r), due to the Doppler shift. If the offset becomes too small, the change in the signal due to the Doppler shift becomes smaller since the Doppler-broadened lineshape will overlap the etalon transmission peak.

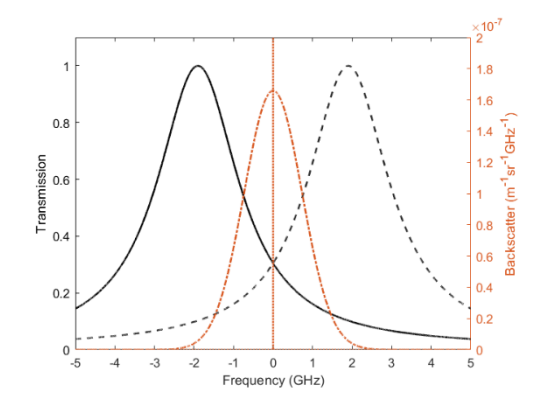


Fig. 3. The etalon transmission for etalons with an FWHM bandpass of 2.5 GHz and a frequency offset of ± 1.9 GHz are shown as the black solid and dashed lines. The molecular backscatter as a function of frequency is shown as the red dot-dashed line, while the aerosol backscatter is represented by the red dotted vertical line.

With the backscatter ratio set to B = 1 so that the signal results solely from molecular backscatter, the Doppler direct detection signal becomes

319
$$M_m(r) = \frac{\int g(r, f_0 + \Delta f, f) \left(\varepsilon_a T_{e,a}(f) - \varepsilon_b T_{e,b}(f)\right) df}{\int g(r, f_0 + \Delta f, f) \left(\varepsilon_a T_{e,a}(f) + \varepsilon_b T_{e,b}(f)\right) df}.$$
 (12)

A plot of the Doppler direct detection signal, $M_m(r = 37.5 m)$, as a function of radial wind speed, is shown in Fig. 4. The black solid, red dashed, and blue dotted lines represent a 0.5-GHz, 1.5-GHz, and 2.5-GHz FWHM etalon bandpass, respectively, with the offset for each set at 1.7 GHz.

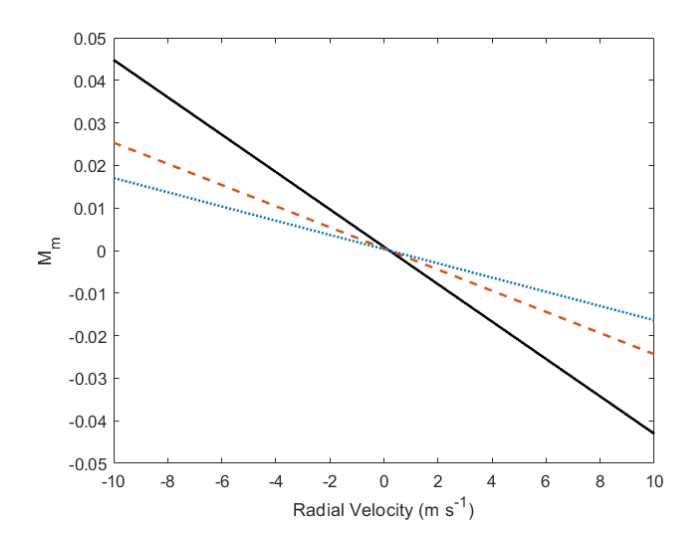


Fig. 4. A plot of the Doppler direct detection signal, $M_m(r = 37.5 m)$, as a function of radial wind speed. The black solid (red dashed, blue dotted) line corresponds to an etalon FWHM bandwidth of 0.5 GHz (1.5 GHz, 2.5 GHz). The slope of the above plot is the sensitivity of the Doppler wind lidar.

The sensitivity, $s_m(r)$, is defined as $s_m(r) = dM_m/dv_r$ and is shown as a function of offset in Fig. 5 for etalon FWHM bandwidths ranging between 0.5 GHz and 3 GHz. As expected, the narrower bandwidths have a higher sensitivity, and the peak sensitivity occurs for offsets between 1.7 GHz for the FWHM bandwidth of 0.5 GHz and 2.1 GHz for the FWHM bandwidth of 3.0 GHz.

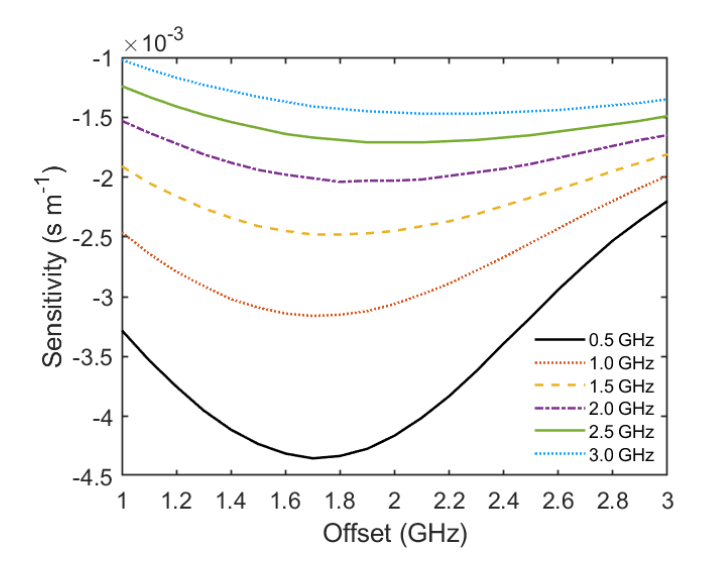
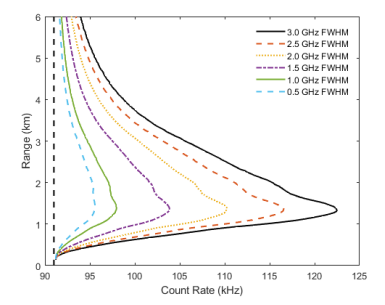


Fig. 5. A plot of the sensitivity as a function of frequency offset is shown for an etalon FWHM bandpass ranging between 0.5 and 3 GHz. The maximum sensitivity occurs between a frequency offset of 1.7 GHz for the etalon FWHM bandpass of 0.5 GHz and an offset of 2.1 GHz for the etalon bandpass of 3.0 GHz. As expected, the narrower etalon bandpass produces a larger sensitivity.

The sensitivity of the DLB Doppler wind lidar receiver is one consideration in the instrument design. This sensitivity must be balanced against the SNR of the return signal, which will also be affected by the choice of the etalon transmission bandwidth and offset. For

the DLB MPD instruments, the SNR primarily results from Poisson noise associated with photon counting statistics. Other error sources will be considered in the next section.

The retrieved SNR can be estimated based on the modeling of the return signal using the instrument parameters listed in Table 1 and the atmospheric model described in section 2. For a five-minute averaging time and a 150-m range bin width, the return count rate as a function of range are shown in the left-hand plot of Fig. 6 for etalon FWHM bandwidths ranging between 0.5 GHz and 3.0 GHz. The offset count rate of 91 kHz results from the background counts based on a solar radiance of $1.15x10^{-3} W cm^{-2} \mu m^{-1} Sr^{-1}$ and a dark count rate of 200 Hz. The SNR resulting from Poisson noise is shown in the right-hand plot of Fig. 6 for etalon FWHM bandwidths ranging between 0.5 GHz and 3.0 GHz. As expected, the narrower etalon bandwidths result in lower SNRs.



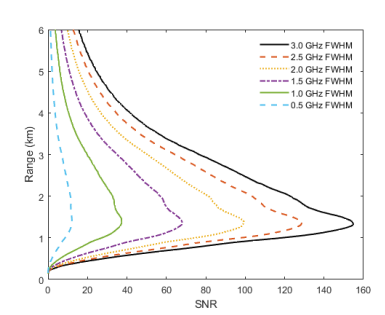
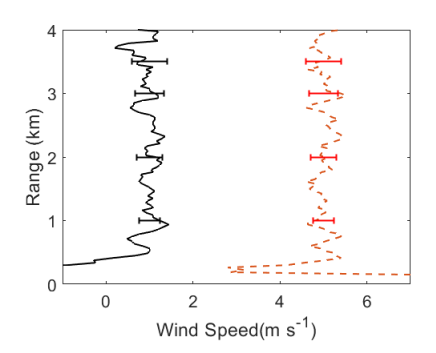


Fig. 6. The left-hand plot shows the return counts as a function of range for the DLB instrument architecture for etalon FWHM bandwidths ranging between 0.5 GHz and 3.0 GHz. The black dashed vertical line represents the 91 kHz count rate associated with the background. The dark count rate is 0.2 kHz. The corresponding SNR as a function of range associated with Poisson noise resulting from photon counting is shown in the right-hand plot. An averaging time of five minutes, a pulse duration of 1 μ s, and a range bin width of 150 m were used.

The retrieved vertical velocity as a function of range is shown in the left-hand plot in Fig. 7 for a 1-m s⁻¹ and 5-m s⁻¹ modeled vertical velocity. This retrieval was based on an etalon FWHM bandpass of 2.5 GHz and a frequency offset of 1.9 GHz. A five-minute averaging time was assumed in the model. The effect of the Poisson noise on the retrieved signal causes the noise associated with the retrieved vertical velocity. The large error below 500 m results from the low signal due to the overlap function (Spuler et al. 2015). However, a wide field of view receiver can be added to achieve vertical wind velocity retrievals below 500 m. The right-hand plot in Fig. 7 shows a histogram of the retrieved vertical velocity for twenty profiles, each with a 1-m s⁻¹ vertical velocity. Each profile used in this histogram ranged between .49 km and 4.2 km, with data points calculated every 37.5 m and each profile providing one hundred data points. The mean and standard deviation for the distribution seen in the histogram is 0.989 m s⁻¹ and 0.333 m s⁻¹, respectively. The mean value represents the

average value of all the retrieved velocities and represents an estimate of the systematic error. The standard deviation represents the variation in the retrieved velocities and provides an estimate of the random error in the velocity retrieval due to the Poisson noise. A summary of the mean and standard deviation for etalon FWHM bandwidths ranging from 0.5 GHz to 3.0 GHz is shown in Table 2. While the narrower etalon bandwidth has a higher sensitivity, the SNR is lower. This higher SNR results in a higher standard deviation in the retrieved vertical velocity profile for the etalon FWHM bandwidth of 0.5 GHz. The etalon bandwidth of 2.5 GHz produces the smallest standard deviation and will be used in the modeling in the remainder of this paper.



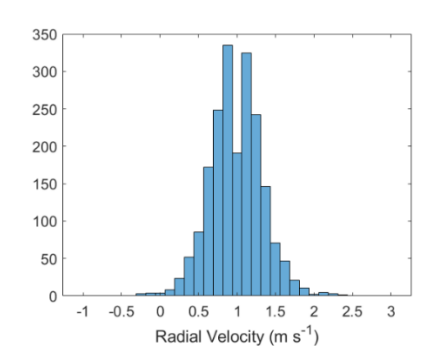


Fig. 7. The left-hand plot shows the modeled retrieved vertical velocity as a function of range for velocities of 1 m s⁻¹ (black solid line) and 5 m s⁻¹ (red dashed line). The right-hand plot shows a histogram of the retrieved vertical velocity as a function of range based on twenty retrieved vertical velocity profiles. A 1-m s⁻¹ vertical velocity was used in the atmospheric model.

Etalon FWHM	Frequency Offset	Mean	Standard Deviation
Bandwidth (GHz)	(GHz)	$(m s^{-1})$	$(m s^{-1})$
0.5	1.7	1.001	0.501
1.0	1.7	0.999	0.390
1.5	1.7	1.007	0.366
2.0	1.8	1.015	0.352
2.5	1.9	0.989	0.333
3.0	2.1	0.997	0.355

Table 2. The mean and standard deviation as a function of the etalon bandwidth and frequency offset.

5. Other sources of error

Poisson noise associated with the photon counting used in the DLB architecture is one major source of uncertainty in the retrieved vertical velocity. Other sources of error in the retrieved vertical velocity can result from the direct detection Doppler lidar instrument and include the stability of the laser transmitter and the etalons. The accuracy of the ancillary measurement of the backscatter ratio, B(r), will also affect the accuracy of the retrieved vertical velocity. Finally, in the retrieval, the Doppler lineshape is needed. This Doppler lineshape depends on the atmospheric temperature profile, and uncertainty in the temperature

profile will translate into uncertainty in the vertical velocity retrieval. These errors are 395 discussed below.

a. Laser transmitter stability

394

396

397

398

399

400

401

402

403

404

405

406

407

408

409

410

411

412

413

414

415

416

417

418

419

420

421

422

423

424

The effects of the laser stability on the retrieved vertical velocity can be estimated by taking the derivative of the Doppler shift with respect to the vertical velocity. This results in the expression $df/dv_r = 2f_0/c$. However, at 780 nm, the resolution of the wavemeter is 49 MHz, corresponding to an uncertainty in the retrieved vertical velocity of 18 m s⁻¹. The laser transmitter needs to have a stability of better than 0.50 MHz to achieve an uncertainty in the retrieved vertical velocity of less than 0.2 m s⁻¹. It should be noted that shifting the frequency of the return spectrum by 0.50 MHz results in an error of the retrieved wind velocity of 0.2 m s⁻¹ which is consistent with the error estimate using the expression $df/dv_r = 2f_0/c$.

The scheme proposed to achieve the needed frequency stabilization is shown schematically in Fig. 2. The wavemeter is used to provide feedback to control the operating temperature of the DBR laser and will provide long-term stability, as has been demonstrated with the current MPD instruments. The wavemeter will provide stabilization of the DBR laser to within 49 MHz of a set operational wavelength. A heated Rb vapor cell will be used to provide an atomic reference near 780 nm, and the Pound-Drever-Hall (PDH) locking technique will be employed to achieve the needed peak frequency stability of 0.50 MHz (Drever et al. 1983). The PDH locking technique utilizes an electro-optic modulator to provide sidebands to the laser spectrum. The laser beam passes through the reference cell, and a detector monitors the signal. The detected signal is then beat against a local oscillator to generate an error signal that can be used to lock the laser operating wavelength to the atomic absorption feature of interest. The PDH locking technique can provide the needed 0.50 MHz frequency stability. Using the wavemeter for the coarse stabilization provides a simple method of stabilizing the laser near the needed operating wavelength by providing larger corrections at a low bandwidth. This coarse locking mechanism is potentially beneficial for long-term unattended operations where environmental conditions may cause the laser to make large frequency excursions that cannot be corrected using the PDH locking technique. The higher bandwidth PDH locking technique can then be optimized to make small frequency corrections to maintain the needed 0.50 MHz frequency stabilization. The goal is to incorporate the proposed Doppler wind lidar with the water vapor MPD, temperature

MPD, and the HSRL, which already use a wavemeter. Since the MPD instruments already use wavemeters, they will be taken advantage of and used for coarse wavelength locking.

b. Etalon stability

The etalons will utilize a solid fused silica substrate with a coefficient of thermal expansion of $0.52 \times 10^{-6} \, \text{K}^{-1}$ for the temperature range of 5 C to 35 C and an index of refraction of 1.4537 at a wavelength of 780 nm. The estimated error in the velocity retrieval was calculated by determining the shift of the resonant wavelength of both etalons based on a temperature deviation, ΔT . The retrieval algorithm is then used with both etalon transmission peaks shifted in the same direction to provide a retrieved temperature using an atmospheric model with an input velocity of 0 m s⁻¹. A plot of the estimated error in the retrieved velocity as a function of temperature deviation is shown in Fig. 8. To maintain an error of less than $0.4 \, \text{m s}^{-1}$, the temperature stability of the etalons needs to be better than 5 mK. This temperature stability will be hard to achieve, and care must be taken in the design of the temperature-stabilized mounts for the etalons.

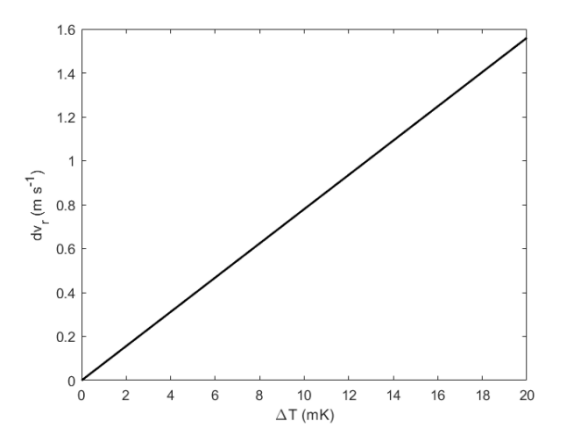


Fig 8. The error in the velocity retrieval as a function of the temperature stability of the etalons. A temperature stability of 5 mK will result in an error of less than 0.4 m s⁻¹.

A second error estimate based on the thermal expansion resulting in the temperature deviation was done using a wind velocity of 1 m/s. Using a temperature deviation of 5 mK, the retrieved error when both etalons are shifted in the same direction is 0.39 m s⁻¹. When the etalons are shifted in the opposite directions, the error in the retrieved velocity is much smaller and approaches zero. This indicates that the results in Fig. 8 represent the maximum error that would be associated with the temperature stability of the etalons.

c. Uncertainty due to the backscatter ratio

The vertical velocity retrieval discussed in section 2 requires an ancillary measurement of the backscatter ratio using the HSRL technique. MPD instruments have demonstrated HSRL measurements of the backscatter ratio, B(r), with an error of less than 5% (Hayman and Spuler 2017). To see how this uncertainty affects the vertical velocity retrieval, we can start by taking the derivative of (8) so that

$$454 dM(r) =$$

$$455 \quad \left[\frac{\left(\varepsilon_a T_{e,a}(f = f_0 + \Delta f) - \varepsilon_b T_{e,b}(f = f_0 + \Delta f)\right) - M(r)\left(\varepsilon_a T_{e,a}(f = f_0 + \Delta f) + \varepsilon_b T_{e,b}(f = f_0 + \Delta f)\right)}{\left(B(r) - 1\right)\left(\varepsilon_a T_{e,a}(f = f_0 + \Delta f) + \varepsilon_b T_{e,b}(f = f_0 + \Delta f)\right) + \int g(r, f_0 + \Delta f, f)\left(\varepsilon_a T_{e,a}(f) + \varepsilon_b T_{e,b}(f)\right) df} \right] dB(r)$$

$$(13)$$

456 From (13), the error in the retrieved velocity can then be found using

$$457 dv_r(r) = \frac{dv_r(r)}{dM(r)} dM(r) =$$

$$458 \quad \frac{dv_{r}(r)}{dM(r)} \left[\frac{\left(\varepsilon_{a}T_{e,a}(f=f_{0}+\Delta f)-\varepsilon_{b}T_{e,b}(f=f_{0}+\Delta f)\right)-M(r)\left(\varepsilon_{a}T_{e,a}(f=f_{0}+\Delta f)+\varepsilon_{b}T_{e,b}(f=f_{0}+\Delta f)\right)}{(B(r)-1)\left(\varepsilon_{a}T_{e,a}(f=f_{0}+\Delta f)+\varepsilon_{b}T_{e,b}(f=f_{0}+\Delta f)\right)+\int g(r,f_{0}+\Delta f,f)\left(\varepsilon_{a}T_{e,a}(f)+\varepsilon_{b}T_{e,b}(f)\right)df} \right] dB(r). \quad (14)$$

In (14), $dv_r(r)/dM(r)$ can be calculated using the atmospheric model. The calculated error in the retrieved vertical velocity, $dv_r(r)$, as a function of range is shown in Fig. 9 for assumed radial velocities of 1 m s⁻¹ and 10 m s⁻¹ as the black solid line and red dashed line, respectively. The blue dot-dashed line represents the backscatter ratio and is shown for reference. The atmospheric model discussed in section 2 and a 5% error in the retrieved backscatter ratio were used for this calculation. In the calculation for the error in the retrieved velocity resulting from error in the retrieved backscatter ratio, dB was estimated by multiplying B(r) by the 5% error. Both M(r) and dB will thus have a dependence on the backscatter ratio. Furthermore, $dv_r(r)/dM(r)$ will also change with range. The interplay of the dependence of these terms as a function of backscatter and range gives rise to the shape of the retrieved velocity error as a function of range and backscatter ratio.

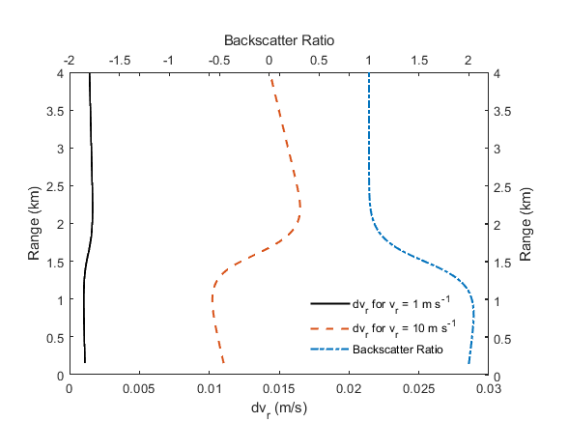


Fig. 9. The error in the retrieved vertical velocity as a function of range due to uncertainty in the ancillary measurement of the backscatter ratio. The black solid and red dashed lines represent nominal radial wind velocities of 1 m s⁻¹ and 10 m s⁻¹, respectively. The blue dot-dashed line represents the backscatter ratio and is shown for reference.

d. Uncertainty in the atmospheric parameters used in the vertical velocity retrieval

The retrieval of the vertical velocity requires calculating $dv_r(r)/dM(r)$ based on atmospheric parameters, including the measured backscatter ratio and an assumed temperature profile, $T(r) = T_S + \gamma r$, where T_S is a measured surface temperature, and γ is the lapse range which typically ranges between -5 K km⁻¹ to -10 K km⁻¹. The temperature profile is then used to estimate the Doppler-broadened lineshape and the molecular backscatter profile needed to complete the vertical velocity retrieval. Differences between the actual and assumed temperature profiles could lead to errors in the retrieved vertical velocity.

The estimate of the error resulting from the assumed temperature profile is calculated in the following manner. A temperature profile with a lapse rate of $\gamma = -6.5~K~km^{-1}$ is assumed. The Doppler direct detection signal, $M(r, \gamma = -6.5~K~km^{-1})$, and the range resolved slope of the velocity profile, $dv_r(r, \gamma = -6.5~K~km^{-1})/dM(r, \gamma = -6.5~K~km^{-1})$, are generated from this temperature profile. Then the lapse rate is changed, and the direct detection signal, $M(r, \gamma)$, is calculated. The error in the retrieved vertical velocity, dv_r , is estimated by (15).

$$dv_r = \frac{dv_r(r, \gamma = -6.5 \, K \, km^{-1})}{dM(r, \gamma = -6.5 \, K \, km^{-1})} (M(r, \gamma) - M(r, \gamma = -6.5 \, K \, km^{-1}))$$
 (15)

A plot of dv_r as a function of range is shown in Fig. 10. The solid lines represent a lapse rate of $\gamma = -5 \ K \ km^{-1}$, and the dashed lines represent a lapse rate of $\gamma = -10 \ K \ km^{-1}$. The black and red lines represent a vertical velocity of 1 m s⁻¹ and 10 m s⁻¹, respectively.

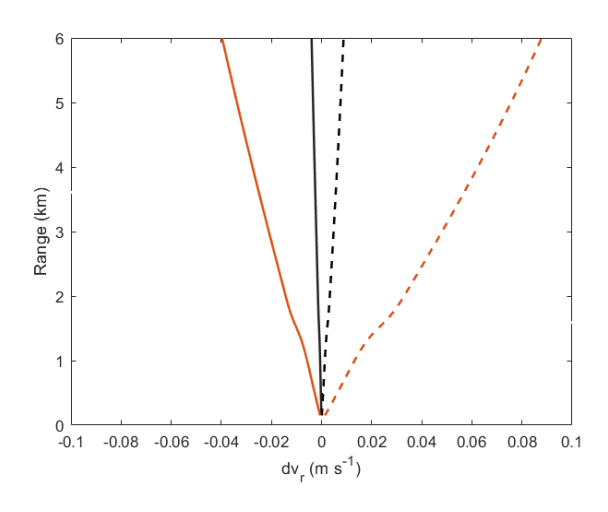


Fig. 10. The error due to uncertainty in the temperature profile as a function of range is shown. The black and red solid lines indicate the error when a -5-K km $^{-1}$ lapse rate was used in the retrieval for a 1-m s $^{-1}$ and 10-m s $^{-1}$ modeled vertical velocity. The black and red dashed lines indicate the error when a lapse rate of -10 K km $^{-1}$ was used in the retrieval for a 1-m s $^{-1}$ and 10-m s $^{-1}$ modeled vertical velocity. The lapse rate used for the atmospheric model was -6.5 K km $^{-1}$.

e. Discussion

The direct detection Doppler wind lidar modeled in this paper is based on the successful architecture that has been employed in the current MPD instruments for water vapor, temperature, and aerosol profiling. These instruments have been developed for autonomous long-term field deployment and fill a need for low-cost ground-based instruments capable of quantitative profiling in the lower troposphere. This paper presents the design for the DLB direct detection Doppler wind lidar that has the potential to add the important capability for vertical wind measurements to the current MPD network.

The error in the vertical velocity retrieval results from several sources. The first source of noise considered in the vertical wind velocity retrieval is the Poisson noise associated with photon counting in the optical receiver. The Poisson noise leads to an error in the vertical wind velocity retrieval of 0.33 m s⁻¹. One potential avenue of decreasing error in the vertical velocity retrieval involves increasing the averaging time. However, as the averaging time increases, it becomes harder to capture the temporal changes in the vertical wind velocity. A second potential avenue to decrease the error in the vertical velocity retrieval is to apply the Poisson Total Variance method (Marais et al. 2006; Hayman et al. 2020). This retrieval method uses a Poisson noise model and imposes a piecewise continuity in time and range to improve the MPD retrievals. It has been successfully applied to the MPD water vapor retrieval, where it increased the maximum range of the retrieved water vapor profile from approximately 4 km to over 6 km (Hayman et al. 2020).

The second source of error in the vertical velocity retrieval results from the laser transmitter frequency stability. Frequency stability of the laser transmitter of 0.50 MHz leads to a 0.2-m s⁻¹ error in the vertical velocity retrieval. Using the Pound-Drever-Hall locking technique (Drever et al. 1983) will achieve this needed laser transmitter stability. Careful implementation of a frequency locking scheme can lead to better locking stability and reduce the error in the vertical velocity retrieval due to the laser frequency stability. However, the complexity of the locking scheme, particularly for field instruments, must be weighed against the improvement to the retrieved vertical velocity.

The third source of error results from the proposed etalon's temperature stability using a commercial temperature controller. This temperature stability led to an error in the vertical velocity retrieval of 0.40 m s⁻¹. The current MPD instruments use etalons similar to those proposed for the direct detection Doppler wind lidar. One of the recent advances in the current field-deployable MPD instruments is the ability to close a shutter at the focal point of the telescope transceiver (Spuler et al. 2021). The diffuse reflection from this shutter is collected into the receiver at the transmitted wavelength. By scanning the DBR laser, the etalon transmission can be mapped out. A similar setup in the proposed instrument will allow the transmission of the two etalons in the direct detection Doppler wind lidar to be measured over the course of atmospheric observations to minimize any errors associated with the etalon transmission as a function of frequency needed for the vertical velocity retrieval.

The fourth and fifth sources of error discussed result from the uncertainty of the ancillary measurement of the backscatter ratio and uncertainty in the temperature profile. The error in the vertical velocity retrieval resulting from uncertainty in the backscatter ratio is less than 0.02 m s⁻¹ and is largest in regions where the backscatter ratio approaches one. The uncertainty of the temperature profile leads to uncertainty in estimating the Doppler lineshape, which results in errors in the retrieved vertical velocity. The estimated error in the retrieved vertical velocity due to this uncertainty is 0.10 m s⁻¹. Incorporating temperature profiles from an operational MPD instrument can help reduce these errors. Since each of these error terms described above are independent, adding the errors in quadrature results in a total error in the retrieved vertical velocity of 0.56 m s⁻¹. A summary of the error budget is provided in Table 3.

Error Source	Error	Contribution to
		Total Error
Poisson Noise	0.33 m s ⁻¹	34.1%
Laser Stability	0.20 m s ⁻¹	12.5%
Etalon Stability	0.40 m s^{-1}	50.1%
Uncertainty in the Aerosol Backscatter	0.02 m s^{-1}	0.2%
Uncertainty in the Atmospheric Parameters	0.10 m s^{-1}	3.1%
Total Error (added in quadrature)	0.56 m s ⁻¹	

Table 3. The error budget for the proposed instrument.

The MPD architecture utilizes existing diode lasers, TSOAs, and other commercially available components that have allowed the successful development of instruments capable of measuring water vapor and temperature in the lower atmosphere. This architecture has also

been used to develop HSRL instruments for measuring aerosol backscatter profiles. These instruments are cost-effective compared to other lidar and DIAL instruments capable of providing quantitative profiling. Furthermore, these instruments have demonstrated long-term unattended operation with a network of five instruments providing continuous data over a three-month period and one instrument providing continuous data for over one year. While the proposed instrument builds on the success of the MPD architecture, this architecture also has limitations that must be considered in the instrument design.

554

555

556

557

558

559

560

561

562

563

564

565

566

567

568

569

570

571

572

573

574

575

576

577

578

579

580

581

582

583

One of the difficulties with using direct detection Doppler wind lidar for measuring line of sight wind velocity is the spectral distribution of the backscatter signal. Several methods for accounting for the spectral distribution of the scattered light can be considered. First, moving to a shorter laser wavelength can increase the molecular backscatter signal. By moving from an operating wavelength of 780 nm to 355 nm, the molecular backscatter signal would increase by a factor of 23. However, this option is not available for the MPD instruments because diode lasers and semiconductor optical amplifiers are commercially available in the red and near-infrared spectral region and because SPCMs are limited to the spectral region below 1 µm. The potential spectral region for the MPD instruments is limited to between 700 nm and 1 µm. A second option for working with the spectral distribution of the backscatter signal is to use an optical filter such as an absorption cell to remove the aerosol backscatter signal. The remaining Doppler-broadened molecular backscatter signal would have a lineshape that can be estimated using a modeled atmosphere. A plot of the Doppler-broadened molecular signal as a function of wavelength is shown in Fig. 11 as the dot-dashed blue line. The transmission measured through the K-cell used in the current HSRL instruments as a function of wavelength is shown as the red dashed line. This measurement was taken by blocking the outgoing beam before the telescope which scatters a small amount of light into the detector. The DBR laser is then scanned in wavelength allowing the transmission scan to be completed. The portion of the backscatter signal transmitted through the K-cell is shown as the black solid line. The molecular backscatter signal transmitted through the K-cell is significantly attenuated due to the atomic absorption. This absorption would greatly reduce the signal seen by the MPD instrument, which would hinder the instrument's performance.

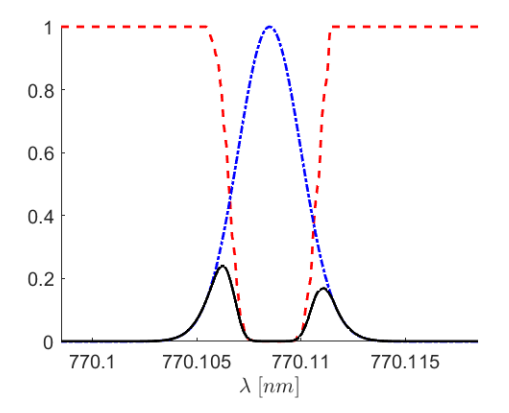


Fig. 11. A plot of the Doppler-broadened molecular backscatter signal as a function of wavelength is shown as the dot-dashed blue line, the K-cell transmission as a function of wavelength as the dashed red line, and the transmitted molecular backscatter signal as a function of wavelength through the K-cell as the black solid line.

The proposed method of using the HSRL measurement to account for the spectral distribution of the backscatter signal allows for the largest signal possible for the proposed MPD instrument. Since these instruments are photon counting instruments, maintaining the largest possible signal is essential for maintaining acceptable instrument performance. The current MPD instrument used for temperature profiling incorporates a water vapor DIAL channel, an O₂ DIAL channel for temperature profiling, and an HSRL channel for aerosol profiling. The temperature measurement relies on the ancillary HSRL measurement of the aerosol backscatter ratio to incorporate the spectral distribution of the backscatter signal into the temperature retrieval and has been successfully demonstrated. The proposed method for vertical wind velocity profiling discussed in this paper builds on the strengths of the MPD architecture to allow multiple measurements to be made with a single instrument while maximizing the measured return signal for these photon counting instruments.

The ability to measure the vertical wind velocity can add a capability to the MPD instruments. It is envisioned that initial wind measurement capabilities will focus on vertical wind profiling that can be used to complement the existing humidity, temperature, and aerosol profiling. Current research efforts are focused on incorporating the existing profiling capabilities into numerical weather forecasting models to improve the predictive capability of these models at the mesoscale. The ability to add vertical winds will provide another important variable to help understand convective processes and provide another boundary condition for the numerical weather forecasting models. Further research efforts will also consider how to effectively scan the proposed lidar instrument to create 3D wind field measurements.

6. Conclusions

611

612	The collaborative effort between MSU and NCAR has led to the development of low-cost
613	ground-based networkable instruments capable of long-term monitoring of the water vapor,
614	temperature, and aerosol distribution in the lower troposphere. The DLB architecture used in
615	these MPD instruments provides an opportunity to add capabilities such as wind
616	measurements. A direct detection Doppler wind lidar design was presented based on the DLB
617	architecture. Furthermore, a retrieval technique for the vertical wind velocity that takes
618	advantage of the ancillary measurement of the backscatter ratio based on the HSRL technique
619	was also presented. The results of this initial modeling indicate that vertical velocity
620	measurements are possible within the lower 4 km of the atmosphere in both the boundary
621	layer and in the free troposphere above the boundary layer with a 0.56-m s ⁻¹ accuracy based
622	on a five-minute averaging time and a 150-m range resolution.
623	Acknowledgments
624	The work was supported by the National Science Foundation through grant #1917851.
625	Data Availability Statement
626	The modeling program used for this work is available by contacting the corresponding
627	author.
628	REFERENCES
629	Abdelazim, S., D. Santoro, M.F. Arend, F. Moshary, and S. Ahmed, 2015: Development and
630	operational analysis of an all-fiber coherent Doppler lidar system for wind sensing and
631	aerosol profiling. IEEE Trans. Geosci. and Remote Sens., 53, 6495-506,
632	https://doi.org/10.1109/TGRS.2015.2442955.
633	Al-Yahyai, S., Y. Charabi, and A. Gastli, 2010: Review of the use of numerical weather
634	prediction (NWP) models for wind energy assessment. Renewable Sustainable Energy
635	Rev., 14, 3192-8, https://doi.org/10.1016/j.rser.2010.07.001 .
636	Ando, T., S. Kameyama, and Y. Hirano, 2008: All-fiber coherent Doppler lidar technologies
637	at Mitsubishi Electric Corporation. IOP Conf. Ser.: Earth Environ. Sci., 1, 012011,
638	https://doi.org/10.1088/1755-1315/1/1/012011.
639	Banakh, V.A., and I.N. Smalikho, 2016: Lidar observations of atmospheric internal waves in
640	the boundary layer of the atmosphere on the coast of Lake Baikal. Atmos. Meas. Tech., 9,
641	5239-48, https://doi.org/10.5194/amt-9-5239-2016.

- Bedka, K.M., and Coauthors, 2021: Airborne lidar observations of wind, water vapor, and
- aerosol profiles during the NASA Aeolus calibration and validation (Cal/Val) test flight
- 644 campaign. Atmos. Meas. Tech., 14, 4305-34, https://doi.org/10.5194/amt-14-4305-2021.
- Bell, T.M., B.R. Greene, P.M. Klein, M. Carney, and P.B. Chilson, 2020: Confronting the
- boundary layer data gap: Evaluating new and existing methodologies of probing the lower
- atmosphere. *Atmos. Meas. Tech.*, **13**, 3855-72, https://doi.org/10.5194/amt-13-3855-2020.
- 648 Bilbro, J.W., C. DiMarzio, D. Fitzjarrald, S. Johnson, and W. Jones, 1986: Airborne Doppler
- lidar measurements. *Appl. Opt.*, **25**, 3952-60, https://doi.org/10.1364/AO.25.003952.
- Bruneau, D., 2001: Mach–Zehnder interferometer as a spectral analyzer for molecular
- Doppler wind lidar. *Appl. Opt.*, **40**, 391-9, https://doi.org/10.1364/AO.40.000391.
- Bunn, C.E., K.S. Repasky, M. Hayman, R.A. Stillwell, and S.M. Spuler, 2018: Perturbative
- solution to the two-component atmosphere DIAL equation for improving the accuracy of
- the retrieved absorption coefficient. *Appl. Opt.*, **57**, 4440-50,
- https://doi.org/10.1364/AO.57.004440.
- 656 Cheng, W.Y., Y. Liu, A.J. Bourgeois, Y. Wu, and S.E. Haupt, 2017: Short-term wind forecast
- of a data assimilation/weather forecasting system with wind turbine anemometer
- measurement assimilation. *Renewable Energy*, **107**, 340-51,
- 659 <u>https://doi.org/10.1016/j.renene.2017.02.014.</u>
- 660 Colberg, L., O. Cruikshank, and K.S. Repasky, 2022. Planetary boundary layer height
- retrieval from a diode-laser-based high spectral resolution lidar. J. Appl. Remote Sens.,
- 662 **16**, 024507, https://doi.org/10.1117/1.JRS.16.024507.
- Dai, L., and Coauthors, 2020: Multilevel Validation of Doppler Wind Lidar by the 325 m
- Meteorological Tower in the Planetary Boundary Layer of Beijing. Atmosphere, 11, 1051,
- https://doi.org/10.3390/atmos11101051.
- Drever, R.W., J.L. Hall, F.V. Kowalsk, J. Hough, G.M. Ford, A.J. Munley, and H. Ward,
- 1983: Laser phase and frequency stabilization using an optical resonator. *Appl. Phys. B*:
- 668 Lasers Opt., 31, 97-105, https://doi.org/10.1007/BF00702605.
- 669 Emmitt, G.D., C. O'Handley, S.A. Wood, R. Bluth, and H. Jonsson, 2005: TODWL: An
- airborne Doppler wind lidar for atmospheric research. Amer. Meteor. Soc. Conf., 2nd

- 671 Symposium on Lidar Atmos. Applications, San Diego, CA, Amer. Meteor. Soc., P2.3,
- http://ams.confex.com/ams/pdfpapers/85828.pdf.
- Esselborn, M., M. Wirth, A. Fix, M. Tesche, and G. Ehret, 2008: Airborne high spectral
- resolution lidar for measuring aerosol extinction and backscatter coefficients. *Appl. Opt.*,
- 47, 346-58, https://doi.org/10.1364/AO.47.006734.
- 676 Gentry, B.M., and H. Chen, 2002: Tropospheric wind measurements obtained with the
- Goddard Lidar Observatory for Winds (GLOW): validation and performance. *Proc. SPIE*
- 678 4484, Lidar Remote Sens. for Ind. and Environ. Monit. II, 74-81, San Diego, CA, SPIE,
- https://doi.org/10.1117/12.452802.
- 680 Gentry, B.M., and H. Chen, 2003: Performance validation and error analysis for a direct-
- detection molecular Doppler lidar. Proc. SPIE 4893, Lidar Remote Sens. for Ind. and
- 682 Environ. Monit. III, 287-294, SPIE, Hangzhou, China, https://doi.org/10.1117/12.466526.
- 683 Gentry, B., H. Chen, J. Cervantes, R. Machan, D. Reed, R. Cargo, C. Marx, and P. Jordan,
- 684 2011: Airborne testing of the TWiLiTE direct detection Doppler lidar. 16th Coherent
- 685 Laser Radar Conf., Long Beach, CA,
- https://sti.usra.edu/sites/sti/clrc2011/presentations/Session%209/Summary%20Bruce%20
- 687 Gentry.pdf.
- 688 Grund, C.J., R.M. Banta, J.L. George, J.N. Howell, M.J. Post, R.A. Richter, and A.M.
- Weickmann, 2001: High-Resolution Doppler Lidar for Boundary Layer and Cloud
- Research. J. Atmos. Oceanic Technol., 18, 376-393, https://doi.org/10.1175/1520-
- 691 0426(2001)018<0376:HRDLFB>2.0.CO;2.
- Hair, J.W., and Coauthors, 2008: Airborne high spectral resolution lidar for profiling aerosol
- optical properties. *Appl. Opt.*, **47**, 6734-52, https://doi.org/10.1364/AO.47.006734.
- Hayman, M., and S. Spuler, 2017: Demonstration of a diode-laser-based high spectral
- resolution lidar (HSRL) for quantitative profiling of clouds and aerosols. *Opt. Express*,
- 696 **25**, A1096-110, https://doi.org/10.1364/OE.25.0A1096.
- 697 Hayman, M., W. Marais, R. Stillwell R, S. Spuler, 2020: Poisson Total Variation Denoising
- for Micropulse Water Vapor DIAL. EPJ Web Conf., 237, The 29th Int. Laser Radar
- 699 *Conf.*, 06012, https://doi.org/10.1051/epjconf/202023706012.

- 700 Irgang, T.D., P.B. Hays, and W.R. Skinner, 2002: Two-channel direct-detection Doppler lidar
- 701 employing a charge-coupled device as a detector, *Appl. Opt.*, **41**, 1145-55,
- 702 https://doi.org/10.1364/AO.41.001145.
- 703 Kanitz, T., and Coauthors, 2020: ESA'S Lidar Missions Aeolus and EarthCARE. EPJ Web
- 704 *Conf.*, 237, The 29th Int. Laser Radar Conf., 01006,
- 705 https://doi.org/10.1051/epjconf/202023701006.
- Kavaya, M.J., J.Y. Beyon, G.J. Koch, M. Petros, P.J. Petzar, U.N. Singh, B.C. Trieu, and J.
- Yu, 2014: The Doppler Aerosol Wind (DAWN) airborne, wind-profiling coherent-
- detection lidar system: Overview and preliminary flight results. J. Atmos. Oceanic
- 709 *Technol.*, **31**, 826-42, https://doi.org/10.1175/JTECH-D-12-00274.1.
- Koch, G.J., J.Y. Beyon, B.W. Barnes, M. Petros, J. Yu, F. Amzajerdian, M.J. Kavaya, and
- U.N. Singh, 2007: High-energy 2 µm Doppler lidar for wind measurements. Opt. Eng.,
- 712 **46**, 116201, https://doi.org/10.1117/1.2802584.
- Kosovic, B., and Coauthors, 2020: A comprehensive wind power forecasting system
- 714 integrating artificial intelligence and numerical weather prediction. *Energies*, **13**, 1372,
- 715 https://doi.org/10.3390/en13061372.
- Kovalev, V.A., and W.E. Eichinger, 2004: *Elastic lidar: theory, practice, and analysis*
- 717 *methods*. John Wiley & Sons, 615 pp.
- Marais, W.J., R.E. Hol, Y.H. Hu, R.E. Kuehn, E.E. Eloranta, and R.M. Willett, 2006:
- Approach to simultaneously denoise and invert backscatter and extinction from photon-
- 1720 limited atmospheric lidar observations. *Appl. Opt.*, **55**, 8316-34,
- 721 https://doi.org/10.1364/AO.55.008316.
- McKay, J.A., 1998: Modeling of direct detection Doppler wind lidar. I. The edge technique.
- 723 *Appl. Opt.*, **37**, 6480-6, https://doi.org/10.1364/AO.37.006480.
- National Academies of Sciences, Engineering, and Medicine, 2018: The Future of
- 725 Atmospheric Boundary Layer Observing, Understanding, and Modeling: Proceedings of
- 726 a Workshop. National Academies Press, 58 pp, https://doi.org/10.17226/25138.
- National Research Council, 2009: Observing weather and climate from the ground up: A
- nationwide network of networks. National Academies Press, 250 pp,
- 729 https://doi.org/10.17226/12540.

- 730 National Research Council, 2010: When weather matters: Science and services to meet
- 731 *critical societal needs.* National Academies Press, 198 pp,
- 732 https://doi.org/10.17226/12888.
- Nehrir, A.R., K.S. Repasky, J.L. Carlsten, M.D. Obland, and J.A. Shaw, 2009: Water vapor
- profiling using a widely tunable, amplified diode-laser-based differential absorption lidar
- 735 (DIAL). J. Atmos. Oceanic Technol., **26**, 733-45,
- 736 https://doi.org/10.1175/2008JTECHA1201.1.
- Nehrir, A.R., K.S. Repasky, and J.L. Carlsten, 2011: Eye-safe diode-laser-based micropulse
- differential absorption lidar (DIAL) for water vapor profiling in the lower troposphere. J.
- 739 *Atmos. Oceanic Technol.*, **28**, 131-47, https://doi.org/10.1175/2010JTECHA1452.1.
- Nehrir, A.R., K.S. Repasky, and J.L. Carlsten, 2012: Micropulse water vapor differential
- absorption lidar: transmitter design and performance. *Opt. Express*, **20**, 25137-51,
- 742 https://doi.org/10.1364/OE.20.025137.
- Post M.J., R.A. Richter, R.M. Hardesty, T.R. Lawrence, and F.F. Hall Jr., 1982: National
- Oceanic and Atmospheric Administration's (NOAA) pulsed, coherent, infrared Doppler
- LIDAR-characteristics and data. Proc. SPIE 0300, Phys. Technol. of Coherent Infrared
- 746 *Radar I*, SPIE, 60-65, https://doi.org/10.1117/12.932577.
- Paffrath, U., C. Lemmerz, O. Reitebuch, B. Witschas, I. Nikolaus, and V. Freudenthaler,
- 748 2009: The airborne demonstrator for the direct-detection Doppler wind lidar ALADIN on
- ADM-Aeolus. Part II: Simulations and Rayleigh Receiver Radiometric performance. J.
- 750 Atmos. Oceanic Technol., 26, 2516-30, https://doi.org/10.1175/2009JTECHA1309.1.
- Reitebuch, O., C. Lemmerz, E. Nagel, U. Paffrath, Y. Durand, M. Endemann, F. Fabre, and
- M. Chaloupy, 2009: The airborne demonstrator for the direct-detection Doppler wind
- 753 lidar ALADIN on ADM-Aeolus. Part I: Instrument design and comparison to satellite
- 754 instrument. J. Atmos. Oceanic Technol., 26, 2501-15,
- 755 <u>https://doi.org/10.1175/2009JTECHA1309.1</u>.
- Reitebuch, O., 2012: Wind lidar for atmospheric research. Atmospheric Physics, U.
- 757 Schumann, Ed., Springer, Berlin, Heidelberg, 487-507.
- Reitebuch, O., and Coauthors, 2020: Initial assessment of the performance of the first wind
- 759 lidar in space on Aeolus. EPJ Web Conf., 237, The 29th Int. Laser Radar Conf., 01010,
- 760 <u>https://doi.org/10.1051/epjconf/202023701010</u>.

- Repasky, K.S., C.E. Bunn, M. Hayman, R.A. Stillwell, and S.M. Spuler, 2019: Modeling the
- performance of a diode laser-based (DLB) micro-pulse differential absorption lidar
- (MPD) for temperature profiling in the lower troposphere. *Opt. Express*, **27**, 33543-63,
- 764 https://doi.org/10.1364/OE.27.033543.
- Rodrigo, P.J., and C. Pedersen, 2012: Field performance of an all-semiconductor laser
- 766 coherent Doppler lidar. *Opt. Lett.*, **37**, 2277-9, https://doi.org/10.1364/OL.37.002277.
- Schroeder, P., W.A. Brewer, A. Choukulkar, A. Weickmann, M. Zucker, M.W. Holloway,
- and S. Sandberg, 2020: A Compact, Flexible, and Robust Micropulsed Doppler Lidar. J.
- 769 *Atmos. Oceanic Technol.*, **37**, 1387-402, https://doi.org/10.1175/JTECH-D-19-0142.1.
- Schween, J.H., A. Hirsikko, U. Löhnert, and S. Crewell, 2014: Mixing-layer height retrieval
- with ceilometer and Doppler lidar: from case studies to long-term assessment. *Atmos*.
- 772 *Meas. Tech.*, 7, 3685-704, https://doi.org/10.5194/amt-7-3685-2014.
- Schwiesow, R.L., and M. P. Spowart, 1996: The NCAR airborne infrared lidar system: Status
- and applications. J. Atmos. Oceanic Technol., 13, 4-15, https://doi.org/10.1175/1520-
- 775 <u>0426(1996)013<0004:TNAILS>2.0.CO;2.</u>
- Shen, F., H. Cha, D. Sun, D. Kim, and S.O. Kwon, 2008: Low tropospheric wind
- measurement with Mie Doppler lidar. *Opt. Rev.*, **15**, 204-9,
- 778 https://doi.org/10.1007/s10043-008-0032-x.
- Shipley, S.T., D.H. Tracy, E.W. Eloranta, J.T. Trauger, J.T. Sroga, F.L. Roesler, and J.A.
- Weinman, 1983: High spectral resolution lidar to measure optical scattering properties of
- atmospheric aerosols. 1: Theory and instrumentation. Appl. Opt., 22, 3716-24,
- 782 <u>https://doi.org/10.1364/AO.22.003716</u>.
- 783 Spuler, S.M., K.S. Repasky, B. Morley, D. Moen, M. Hayman, and A.R. Nehrir, 2015: Field-
- deployable diode-laser-based differential absorption lidar (DIAL) for profiling water
- 785 vapor. Atmos. Meas. Tech., 8, 1073-87, https://doi.org/10.5194/amt-8-1073-2015.
- 786 Spuler, S.M., M. Hayman, R.A. Stillwell, J. Carnes, T. Bernatsky, K.S. Repasky, 2021:
- 787 MicroPulse DIAL (MPD) a Diode-Laser-Based Lidar Architecture for Quantitative
- Atmospheric Profiling. Atmos. Meas. Tech., 14, 4593-616, https://doi.org/10.5194/amt-
- 789 14-4593-2021.

- 790 Stillwell, R.A., S.M. Spuler, M. Hayman, K.S. Repasky, and C.E. Bunn, 2020:
- Demonstration of a combined differential absorption and high spectral resolution lidar for
- 792 profiling atmospheric temperature. *Opt. Express*, **28**, 71-93,
- 793 https://doi.org/10.1364/OE.379804.
- 794 Straume, A.G., and Coauthors, 2020: ESA's Space-based Doppler Wind Lidar Mission
- Aeolus-First Wind and Aerosol Product Assessment Results. EPJ Web of Conf., Volume
- 796 *237, 2020, The 29th Int. Laser Radar Conf.*, 01007,
- 797 https://doi.org/10.1051/epjconf/202023701007.
- Tucker, S.C., C.S. Weimer, S. Baidar, and R.M. Hardesty, 2018: The optical autocovariance
- wind lidar. Part I: OAWL instrument development and demonstration. J. Atmos. Oceanic
- 800 *Technol.*, **35**, 2079-97, https://doi.org/10.1175/JTECH-D-18-0024.1.
- Turk, F.J., S. Hristova-Veleva, S.L. Durden, S. Tanelli, O. Sy, G.D. Emmitt, S. Greco, S.Q.
- Zhang, 2020: Joint analysis of convective structure from the APR-2 precipitation radar
- and the DAWN Doppler wind lidar during the 2017 Convective Processes Experiment
- 804 (CPEX). Atmos. Meas. Tech., 13, 4521-37, https://doi.org/10.5194/amt-13-4521-2020.
- Wallace J.M. and P.V. Hobbs, 2006, Atmospheric Science: An Introductory Survey. Elsevier,
- 806 483 pp.
- Weitkamp, C., Ed., 2006. *Lidar: range-resolved optical remote sensing of the atmosphere.*
- 808 Springer Science & Business, 460 pp.
- Werner, C., and Coauthors, 2001: Wind infrared Doppler lidar instrument. Opt. Eng., 40,
- 810 115-25, https://doi.org/10.1117/1.1335530.
- Witschas, B., S. Rahm, A. Dörnbrack, J. Wagner, and M. Rapp, 2017: Airborne wind lidar
- measurements of vertical and horizontal winds for the investigation of orographically
- induced gravity waves. J. Atmos. Oceanic Technol., **34**, 1371-86,
- 814 https://doi.org/10.1175/JTECH-D-17-0021.1.
- 815 Wulfmeyer, V., and Coauthors, 2015: A review of the remote sensing of lower tropospheric
- thermodynamic profiles and its indispensable role for the understanding and the
- simulation of water and energy cycles. Rev. Geophys., 53, 819-95,
- 818 https://doi.org/10.1002/2014RG000476.

Xia, H., D. Sun, Y. Yang, F. Shen, J. Dong, and T. Kobayashi, 2007: Fabry-Perot interferometer based Mie Doppler lidar for low tropospheric wind observation. *Appl. Opt.*, 46, 7120-31, https://doi.org/10.1364/AO.46.007120.
Zhao Q., J. Cook, Q. Xu, and P.R. Harasti, 2006: Using radar wind observations to improve mesoscale numerical weather prediction. *Wea. Forecasting*, 21, 502-22, https://doi.org/10.1175/WAF936.1.